Carbon Letters (2023) 33:2063–2074
https://doi.org/10.1007/s42823-023-00540-0

Online ISSN 2233-4998
Print ISSN 1976-4251

ORIGINAL ARTICLE

Electrostatic self-assembly cellulose nanofibers/MXene/nickel chains for highly stable and efficient seawater evaporation and purification

Shuai Yang[1] · Cai Shi[1] · Keqi Qu[1] · Zhe Sun[1] · Handong Li[2,3] · Benbin Xu[2] · Zhanhua Huang[1] · Zhanhu Guo[2]

Received: 13 March 2023 / Revised: 6 May 2023 / Accepted: 22 May 2023 / Published online: 12 June 2023

Abstract

Seawater evaporation and purification powered by solar energy are considered as a promising approach to alleviate the global freshwater crisis, and the development of photothermal materials with high efficiency is imminent. In this study, cellulose nanofiber (CNF)/MXene/Ni chain (CMN) aerogels were successfully synthesized by electrostatic force and hydrogen bond interaction force. CMN_{10} achieved a favorable evaporation rate as high as 1.85 kg m^{-2} h^{-1} in pure water, and the corresponding evaporation efficiency could be up to 96.04%. Even if it is applied to seawater with multiple interference factors, its evaporation rate can still be 1.81 kg m^{-2} h^{-1}. The superior seawater evaporation activity origins from the promoted separation of photoexcited charges and photothermal conversion by the synergy of Ni chain and MXene, as well as the water transport channel supported by the 3D structure frame of CNF. Most importantly, CMN aerogel can maintain water vapor evaporation rates above 1.73 kg m^{-2} h^{-1} under extreme conditions such as acidic (pH 2) and alkaline (pH 12) conditions. In addition, various major ions, heavy metals and organic pollutants in seawater can be rejected by CMN_{10} during desalination, and the rejection rates can reach more than 99.69%, ensuring the purity of water resources after treatment. This work shows the great potential of CMN aerogel as a high-efficiency solar evaporator and low-cost photothermal conversion material.

Graphical abstract

Cellulose nanofiber (CNF)/MXene/Ni chain (CMN) aerogels demonstrated high evaporation of water from sea water.

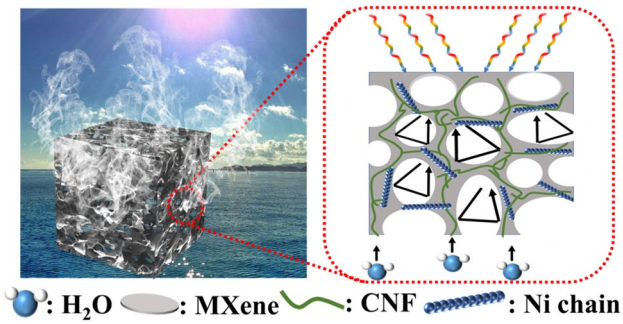

Keywords Ni chain · MXene · Seawater evaporation · Water purification · Solar energy

Shuai Yang and Cai Shi contributed equally to this work.

✉ Zhanhua Huang
huangzh1975@163.com

✉ Zhanhu Guo
zhanhu.guo@northumbria.ac.uk

[1] Key Laboratory of Bio-Based Material Science and Technology, Ministry of Education, College of Material Science and Engineering, Northeast Forestry University, Harbin 150040, China

[2] Mechanical and Construction Engineering, Faculty of Engineering and Environment, Northumbria University, Newcastle Upon Tyne NE1 8ST, UK

[3] College of Materials Science and Engineering, Taiyuan University of Science and Technology, Taiyuan 030024, China

1 Introduction

The global freshwater resource scarcity has triggered a drinking water crisis, which is related to human survival [1–5]. Seawater desalination is considered to be one of the most potential solutions [6, 7]. Solar-driven water evaporation technology has increasingly been recognized as a promising strategy for seawater desalination compared with traditional methods [8–10]. To this end, the development of photothermal conversion materials with enhanced light absorption is the prerequisite for high-efficiency solar water evaporator.

To date, various photothermal materials have been widely used for seawater evaporation, including inorganic semiconductor materials [11, 12], carbon-based materials [13, 14], organic polymers [15, 16], surface plasmon resonance metals [17, 18], etc. Thereinto, two-dimensional MXene nanosheets with large surface areas and broad photo-absorption ability have been widely employed in photocatalysis and photothermal conversion as light absorbers [19, 20]. The photothermal conversion mechanism of MXene is as follows: electrons-holes pairs could be generated in MXene when they were illuminated by photons with energy larger than its band gap potential; excited electrons tend to return to the ground state to bond with holes, converting radiant energy into thermal energy at the same time [21, 22]. However, MXene is prone to agglutination, which not only limits its photothermal conversion capacity but also results in fewer interlayer transport channels for water [23]. This is extremely detrimental to seawater desalination, so it is still urgent to search for a high-efficiency photothermal conversion material.

Studies have shown that the self-assembly of Ni chain and MXene (MXene/Ni) by electrostatic action can not only effectively solve the agglomeration phenomenon of MXene by avoiding the stacking of MXene lamellar, but also further improve the photothermal conversion performance of materials [24]. As a typical plasmon resonance metal, Ni has broadband absorption, the maximum absorption rate of sunlight can be up to 96% [25–27]. Increasing the Ni chains size could further enhance its absorption of solar energy [28, 29], thus improving the photothermal conversion efficiency [14]. However, the hydrophobicity of Ni chains limits the application of MXene/Ni in seawater evaporation. Incorporating cellulose nanofiber (CNF) can effectively improve the hydrophilicity of MXene/Ni because of the abundant –OH on CNF surface [30, 31]. Meanwhile, the three-dimensional (3D) skeleton structure of CNF is conducive to the enhancement of water transport channels in CNF/MXene/Ni chain system.

In this study, CNF/MXene/Ni chain (CMN) aerogel was successfully constructed by electrostatic self-assembly and hydrogen bond crosslinking. Due to the enhanced light absorption and photothermal conversion of Ni chain and MXene, the hydrophilicity of CNF and the abundant porous structure in CMN aerogel, the water evaporation rate of CMN aerogel is significantly improved. CMN aerogel could implement a maximum evaporation rate as high as 1.85 kg m^{-2} h^{-1} in pure water, while 1.81 kg m^{-2} h^{-1} in seawater under one sunlight intensity. Furthermore, the concentration of Ca^{2+}, K^{+}, Na^{+} and Mg^{2+} in seawater could be reduced by CMN to the range required by WHO and the USA for drinking water quality. Some heavy metal ions and organic pollutants could also be effectively rejected and the rejection rate of Rhodamine B and other pollutants is above 99.69%. Therefore, this study provides new methods and ideas for solving the water resources crisis and the development and utilization of solar energy.

2 Experimental

2.1 Sample preparation

2.1.1 Preparation of MXene

In the first step, LiF (1 g) and deionized water (5 mL) were added into 15 mL concentrated hydrochloric acid, followed by adding 1 g Ti_3AlC_2 (MAX) under stirring. After the reaction at 40 °C for 24 h in a water bath, the obtained solution was centrifugally washed at 3500 rpm for several times until neutral. The washed solution was transferred to a conical flask, sonicated for 3 h in an ice water bath. MXene dispersion solution was collected after centrifugation (5000 rpm for 20 min).

2.1.2 Preparation of P-Ni chain

0.594 g of nickel chloride hexahydrate ($NiCl_2{\cdot}6H_2O$) was dissolved in 50 mL ethylene glycol, and then, 1 g of polyvinylpyrrolidone (PVP) and 0.4 g of sodium hydroxide (NaOH) were added into above solution, ultrasonically dispersed for 30 min in an ice water bath. Then, 1.5 mL of hydrazine hydrate ($N_2H_4{\cdot}H_2O$) was dropped into the mixture and continued to the ultrasound for another 10 min. Finally, under the parallel magnetic field, the mixture was bathed in water at 80 °C for 1 h, and Ni chain was obtained after washing centrifugally. Poly diallyl dimethyl ammonium chloride (PDDA 1 wt%) modified Ni chain (P-Ni chain) was achieved by employing PDDA into the aforementioned Ni chain solution with 30 min ultrasound.

2.1.3 Preparation of CMN aerogel

The above-prepared MXene dispersed solution (8.5 mL 10 mg L^{-1}) and P-Ni chain (0, 2.5, 5, 7.5, 10, and 12.5 mg) were added into the CNF solution (1.5 g, 1 wt%) and stirred vigorously for 2 h to obtain the suspension. The mixture was then transferred to a mold, frozen in a refrigerator for 24 h, followed by vacuum freeze-dried (− 78 °C, 20 Pa) for 48 h to get CNF/MXene/Ni chain (CMN) aerogel. The samples with different P-Ni chain contents were synthesized, labeled as CMN_X (X represents the incorporated mass of P-Ni chain (mg), $X = 0$, 2.5, 5, 7.5, 10 and 12.5). Figure 1 shows the preparation process of CMN aerogel.

2.2 Solar desalination test

The evaporation test was conducted at ~ 15 °C and humidity of ~ 45%. Xenon lamp equipped with AM1.5G filter (1 kW m^{-2}, Beijing CEJ Tech. Co., Ltd., Beijing, China) was used as the sunlight simulation light source. In the experiment, the CMN aerogel was cut into a square with an area of 9 cm^2, and the initial water volume was 100 mL. The CMN aerogel deposited foam board (6 cm in diameter) served as light absorber, which was placed on the water surface. The hydrophilic cotton with capillary action was closely contacted with the foam board as a water transportation channel. Under light irradiation, the weight of the balance was recorded every 5 min and lasted for 1 h. The seawater desalination test was conducted with simulated seawater which is configured according to Table S1. All experiments were repeated three times. The water vapor evaporation rate was calculated as follows [32]:

$$\text{Evaporation}\ \left(\text{kg m}^{-2}\ \text{h}^{-1}\right) = \frac{m_t}{S \times t}, \quad (1)$$

where m (kg) represents the change of water mass, S (m^2) represents the actual area of the sample, and t (h) represents the evaporation time of water.

The evaporation efficiency was calculated according to Eqs. (2) and (3) [33, 34]:

$$\eta = \frac{m\left(H_{\text{LV}} + C \times \Delta T\right)}{P_{in}}, \quad (2)$$

$$H_{\text{LV}} = 1.91846 \times 10^6 \left[T/(T - 33.91)\right]^2. \quad (3)$$

In the formula, η (%) represents the evaporation efficiency of the sample, m (kg m^{-2} h^{-1}) is the mass change rate of evaporated water, C (4.18 kJ kg^{-1} K^{-1}) is the specific heat capacity of water, ΔT (K) is the temperature change on the surface of the sample, and P_{in} (kJ m^{-2} h^{-1}) is the optical power density, H_{LV} (kJ kg^{-1}) is the enthalpy of water vapor phase transformation, and T (K) is the evaporation temperature.

In the evaporation process, the surface temperature of the sample is tested and recorded every 30 s by the near-infrared imager (HIKMICRO, H21); in order to test the rejection rate of organic pollutants, the Ultraviolet/Visible/Near-infrared (UV–Vis–NIR) spectrophotometer (Beijing Purkinje TU-1900) was used to select the corresponding maximum absorption peak of pollutants for concentration monitoring, and the corresponding concentration was obtained according to Fig S1.

For the seawater desalination test, the concentrations of Na^+, Ca^{2+}, K^+ and Mg^{2+} in the simulated seawater were 10,780, 410, 380 and 1310 mg L^{-1}, respectively. The pH of simulated seawater was adjusted by HCl and NaOH. 10 mg L^{-1} heavy metal solution and 30 mg L^{-1} organic dye contaminant with simulated seawater as solvent were employed in the pollutant rejection experiments. The rejection rates

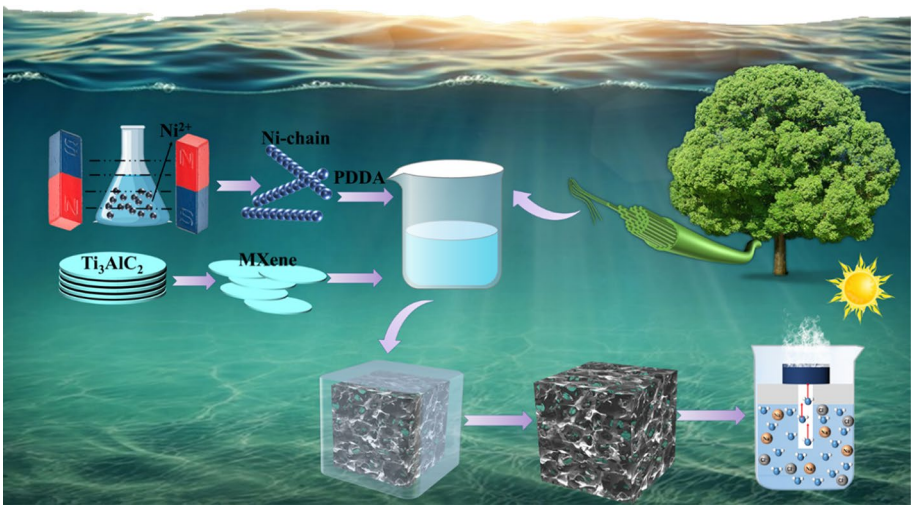

Fig. 1 Schematic synthesis process of CMN aerogel

for metal cations, heavy metal ions, and organic pollutants in seawater were calculated according to Eq. (4):

$$\text{Rejection rates} = \frac{C_1 - C_2}{C_1} \times 100\%. \quad (4)$$

In the formula, C_1 represents the initial concentration of pollutants, and C_2 represents the concentration of pollutants in the condensate.

3 Results and discussion

3.1 Characterization of CMN_x

The microstructure of P-Ni chain, MXene, and CMN_{10} aerogel was observed by scanning electron microscope (SEM) and transmission electron microscope (TEM) (Fig. 2). The P-Ni chain was formed by directional assembly of Ni microspheres, with a diameter of about 150 nm and a length-to-diameter ratio of above 20 (Fig. 2a). The facilitated light absorption by the increased aspect ratio was favorable for improving the photothermal conversion performance of CMN [29]. As shown in Fig. 2b and S2, MAX after etching presented a typical accordion package, and monolayer MXene nanosheets appeared after ultrasonic stripping. The X-ray diffractometer (XRD) patterns of MAX and MXene in Fig. S3 demonstrated the successful synthesis of MXene (the disappearance of the diffraction peak at 38.9° means the removal of Al atomic layer) [35]. The SEM images of CMN_{10} aerogel cross section displayed that the CMN_{10} aerogel maintained the 3D porous honeycomb structure of CNF (Fig. 2c); P-Ni chain was anchored on the MXene lamella by electrostatic force, and MXene nanosheets were attached to the pore walls of CMN_{10} (Fig. 2d). This manifested the CMN_{10} aerogel which was prepared successfully. As shown in Fig. 2e–h, the energy dispersion spectrum (EDS) mapping further verified the successful anchoring of P-Ni chain onto the MXene lamellae and the synthesis of CMN aerogel. Studies have shown that the rich pore structure in a sample can produce multiple reflections of sunlight, thus enhancing the absorption of sunlight [36]. In addition, the rich pore structure also facilitates the rapid escape of water vapor generated, thus increasing the evaporation rate of water vapor of material [37]. The anchoring of P-Ni chain can effectively avoid the stacking of MXene layers and promote the light absorption of CMN. Therefore, CMN aerogel have great potential in solar desalination.

The theoretical feasibility of successful preparation of CMN was demonstrated by Zeta potential (Fig. 3a) and the Fourier transform infrared (FTIR) (Fig. 3b). As exhibited in Fig. 3a, the surface charge of MXene was − 32.6 mV due to the abundant –OH on the surface of it, while + 44.1 mV for P-Ni chain because of the modification of PDDA. Electrostatic self-assembly easily occurs between MXene and P-Ni chain with opposite charges [38]. The abundant –OH on the surface of CNF, MXene, and CMN_{10} were further certified by FTIR spectra (Fig. 3b). In the spectra of CNF and MXene, peaks at 3445 cm^{-1} and 1660 cm^{-1} were observed as –OH stretching vibrations, while the peak at 1050 cm^{-1} was C–O stretching vibration peak. The characteristic peaks of CNF and MXene can be found in the FTIR spectra of CMN aerogels, which indicates the successful complexation

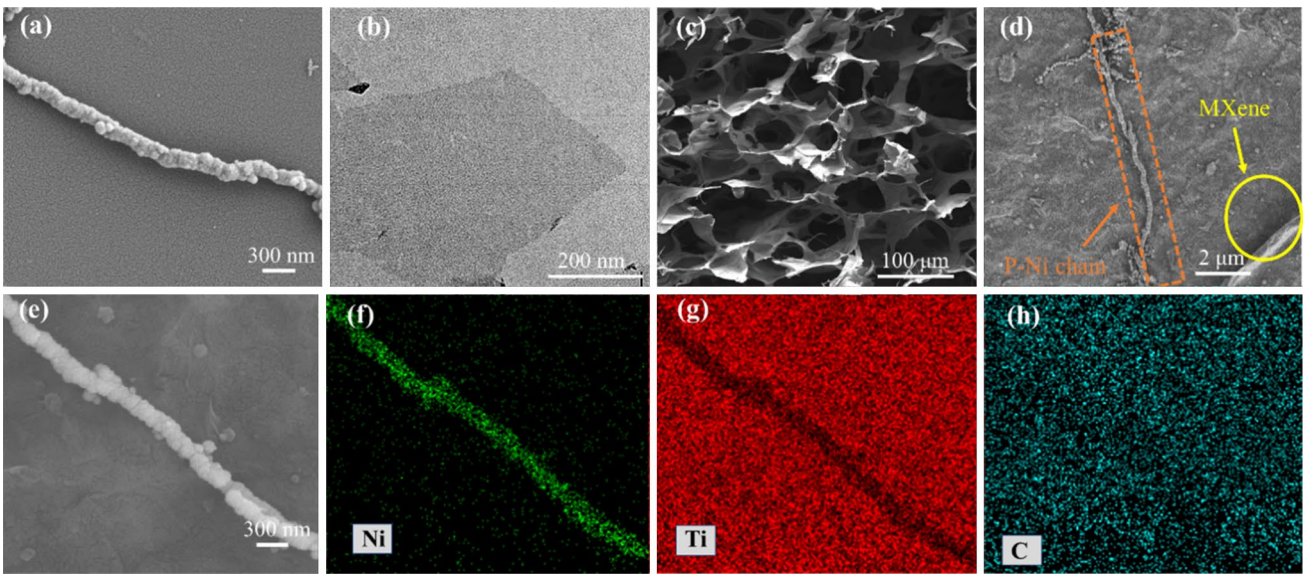

Fig. 2 **a** SEM image of P-Ni chain; **b** TEM image of MXene lamellar; SEM image of **c–e** CMN_{10} aerogel; **f–h** EDS element mapping results for Ni, Ti and C

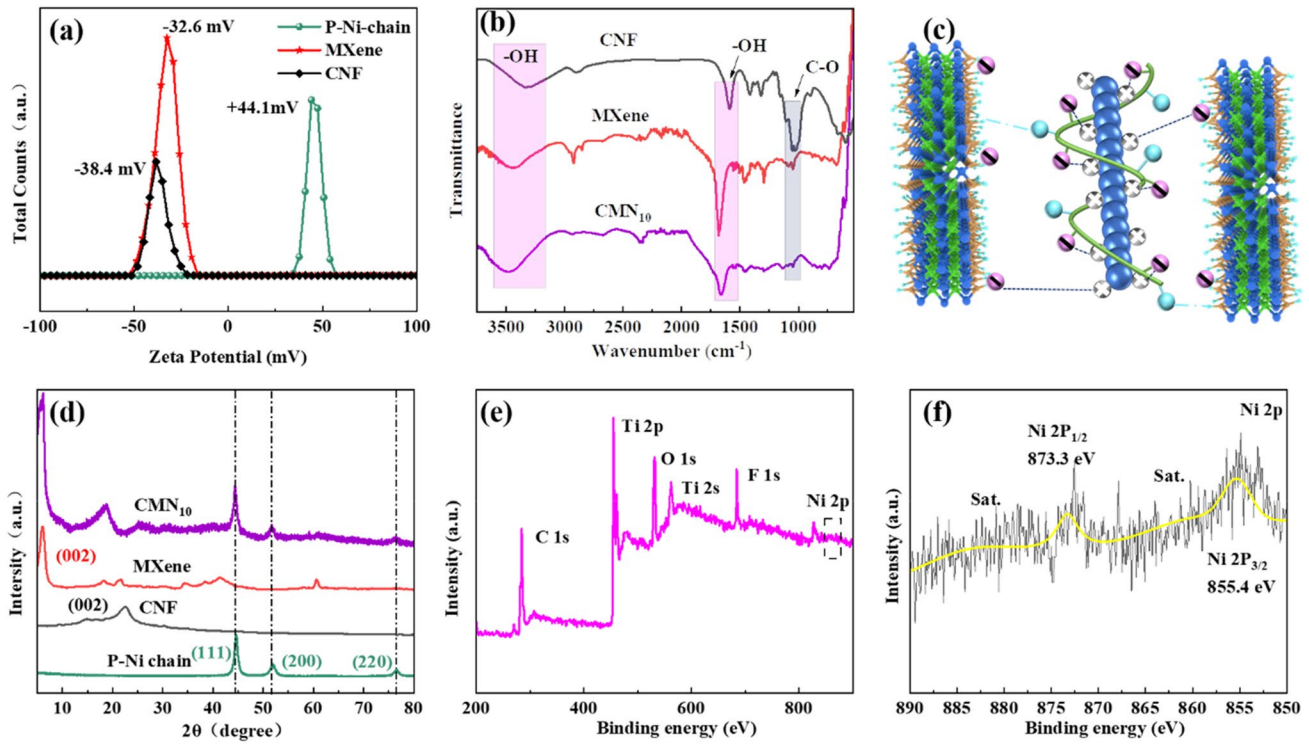

Fig. 3 **a** Zeta potential of MXene nanosheet, CNF and P-Ni chain; **b** FTIR spectra of CMN_{10}, MXene nanosheet and CNF; **c** electrostatic interaction and hydrogen bonding effect among MXene, CNF and P-Ni chain; **d** XRD patterns of CMN_{10}, MXene nanosheet, CNF and P-Ni chain; **e** the XPS spectra and f Ni 2p high-resolution spectra of CMN_{10}

of MXene with CNF [39]. It was observed that the peak position of C–O shifted from 1050 cm^{-1} (in MXene and CNF) to 1040 cm^{-1} (CMN_{10}), which was mainly due to the formation of a large number of intermolecular hydrogen bonds between CNF and MXene [40, 41]. The hydrogen bond interactions formed by –OH crosslinking promoted the close connection between CNF and MXene. Furthermore, the electrostatic interaction between MXene and P-Ni chain as well as the hydrogen bonding effect among MXene and CNF is illustrated in Fig. 3c.

Figure 3d shows the XRD pattern of CMN_{10}, P-Ni chain, CNF and MXene. Compared with MXene, the (002) peak of MXene in CMN_{10} shifted from 6.18° to 5.8°, which is due to the electrostatic force and hydrogen bond among P-Ni chain, MXene, and CNF, leading to the increase in layer spacing in MXene [42]. In addition, peaks at 44.5°, 51.6° and 76.4° in the XRD pattern of CMN_{10} corresponded to (111), (200) and (220) crystal planes of Ni, respectively [43], which means that the P-Ni chain has been successfully reassembled in CMN_{10} by electrostatic self-assembly. The composition and valence structure of the elements in CMN_{10} were explained by X-ray photoelectron spectroscopy (XPS). As shown in Fig. 3e, the coexisting of Ni, C, O, Ti, and F elements in the survey spectrum (Fig. 3e) indicated the successful preparation of CMN_{10}. In the high-resolution XPS spectrum of C 1 s (Fig. S4a), peaks at 288.58, 286.18, 284.58, 282.28, and 281.58 eV were corresponding to O–C=O, C–O, C–C, Ti–C–O, and C–Ti, respectively [44]. As observed in Fig. S4b, the Ti–C $2p_{3/2}$, Ti(II) $2p_{3/2}$, Ti_xO_y $2p_{3/2}$, TiO_2 $2p_{3/2}$, Ti–C $2p_{1/2}$, Ti(II) $2p_{1/2}$, Ti_xO_y $2p_{1/2}$, TiO_2 $2p_{1/2}$ of MXene located at 454.68, 455.28, 456.08, 456.98, 458.08, 460.68, 461.68, and 463.78 eV, respectively [45, 46], indicating that MXene was successfully doped in CMN_{10} and maintains the intrinsic state. The high-resolution spectrum of Ni 2p in Fig. 3f displayed the peaks at 855.38 and 873.08 eV, which were assigned to Ni $2p_{1/2}$ and Ni $2p_{3/2}$, respectively [47]. Figure S5 is the TGA curve of CMN_{10} that demonstrated the excellent thermal stability [48]. Only about 10% mass loss was shown when the temperature was as high as 800 °C.

The light absorption and photothermal conversion of materials are critical to obtaining excellent water evaporation performance [49]. Infrared imaging was performed to detect the surface temperature change of CMN_X ($X = 0$, 2.5, 5, 7.5, 10, and 12.5) under one sun illumination (Fig. 4a). A darker color indicates a higher temperature. As shown in Fig. 4a, the color of CMN_{10} was much darker than other CMN_X ($X = 0$, 2.5, 5, 7.5, and 12.5). The surface temperature of CMN_{10} was as high as 58.5 °C, while only 45.3 °C can be detected on the surface of CMN_0. Nevertheless, the surface temperature of CMN increased first and then decreased with

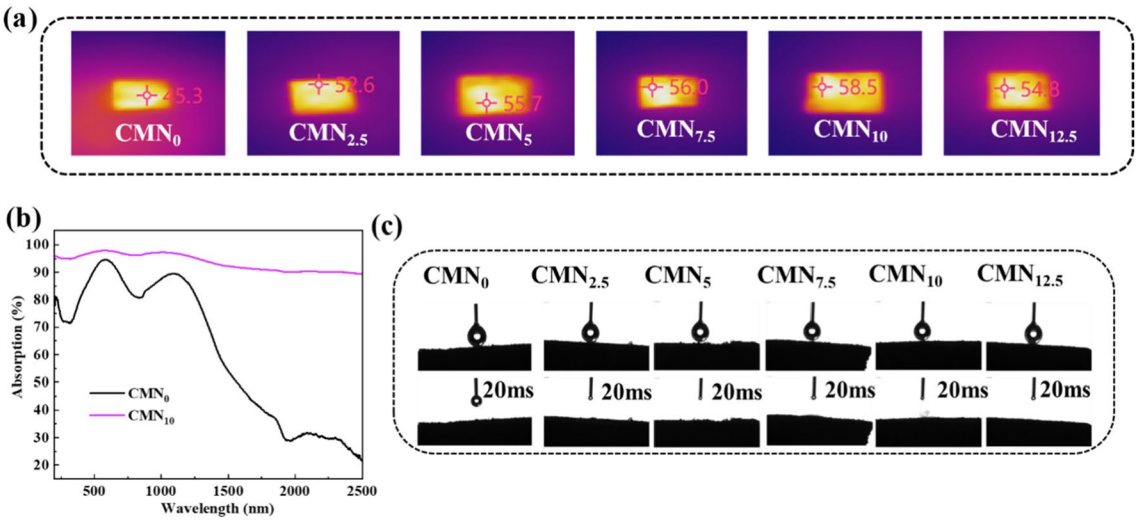

Fig. 4 **a** The infrared image of CMN_x in sunlight; **b** optical absorption spectra of CMN_{10} and CMN_0 in sunlight; **c** water contact angle of CMN_x

the increase in P-Ni chain content. This could be for two reasons: (1) excess P-Ni chain leads to their possible aggregation on the aerogel surface, which increased the sunlight reflection; (2) the heat conduction of CMN was faster when the thermal conductivity increased caused by excess P-Ni chain [50]. The light absorption ability of CMN_0 and CMN_{10} is further tested by UV–Vis NIR spectrophotometer. It can be seen from Fig. 4b that CMN_{10} exhibited full spectrum absorption within the range of 200–2500 nm. The absorption of sunlight by CMN_{10} is up to 95%, while that of CMN_0 is only about 61%. Based on Fig. 4a–b, it can be concluded that the light absorption capacity of CMN is proportional to its photothermal conversion capacity [19].

The hydrophilicity of the sample is another indicator to evaluate the desalination performance of it [51]. As shown in Fig. 4c, water contact angles of CMN_0, $CMN_{2.5}$, CMN_5, $CMN_{7.5}$, CMN_{10} and $CMN_{12.5}$ were carried out to evaluate their hydrophilicity. All the samples were able to absorb the drops within 20 ms after the water drops off because of the abundant –O–H (Fig. S6). Moreover, the addition of P-Ni chain did not affect the hydrophilicity of the sample.

3.2 Solar-powered water evaporation performance of CMNX aerogels

The evaporation rate is the most intuitive indicator to judge the vapor evaporation performance of the samples; therefore, pure water was first used as the evaporation source to test the vapor evaporation performance of CMN aerogel [52]. The water evaporation device is shown in Fig. S7a. The water vapor can be obviously seen on the top of the device in dark (Fig. S7b). Figure 5a reflects the mass changes of water over various CMN under light irradiation. With the irradiation time increased, the mass of all samples decreased, with CMN_{10} being the most pronounced. The evaporation rate of CMN_{10} reached the highest of 1.85 kg m^{-2} h^{-1} (Fig. 5b). However, the evaporation rate of $CMN_{12.5}$ was much lower than CMN_{10}, which was consistent with the light absorption and photothermal conversion properties of the sample (Fig. 4a–b). The reasons for this phenomenon are as follows: (1) the excess Ni chains form a pile-up and lead to an increase in the reflectance of $CMN_{12.5}$ to sunlight, which reduces the photothermal conversion efficiency of $CMN_{12.5}$; (2) the excess addition of Ni chains leads to $CMN_{12.5}$'s thermal conductivity will increase, and the heat generated by the photothermal reaction will be rapidly conducted and dissipated, and cannot be used to heat water and cause a decrease in the evaporation rate of water vapor [50]. The variation trend of the maximum surface temperature of the sample during evaporation (Fig. 5c) is similar to that of the evaporation rate (Fig. 5a, b), and the surface temperature of CMN_{10} is the highest, reaching 40.5 °C. Compared with CMN_X ($X > 0$), the surface temperature of CMN_0 rose slowly, reaching 37.4 °C in about 7 min, which indicated the favorable role of P-Ni chain in promoting the light absorption and photothermal conversion of sample.

Solar evaporation efficiency is also one of key paramenters to measure the performance of water vapor evaporation of materials, which directly reflects the utilization degree of sunlight [53]. It can be observed from Fig. 5d that the solar evaporation efficiency was also positively correlated with the water vapor evaporation rate. The solar evaporation efficiency of CMN_{10} reached up to 96.04%, much higher than that of CMN_0. The stability test showed the excellent cyclic stability in evaporation performance of CMN_{10} (Fig. S8). This could be attributed to the synergy of electrostatic and hydrogen bond interaction among CNF, MXene, and

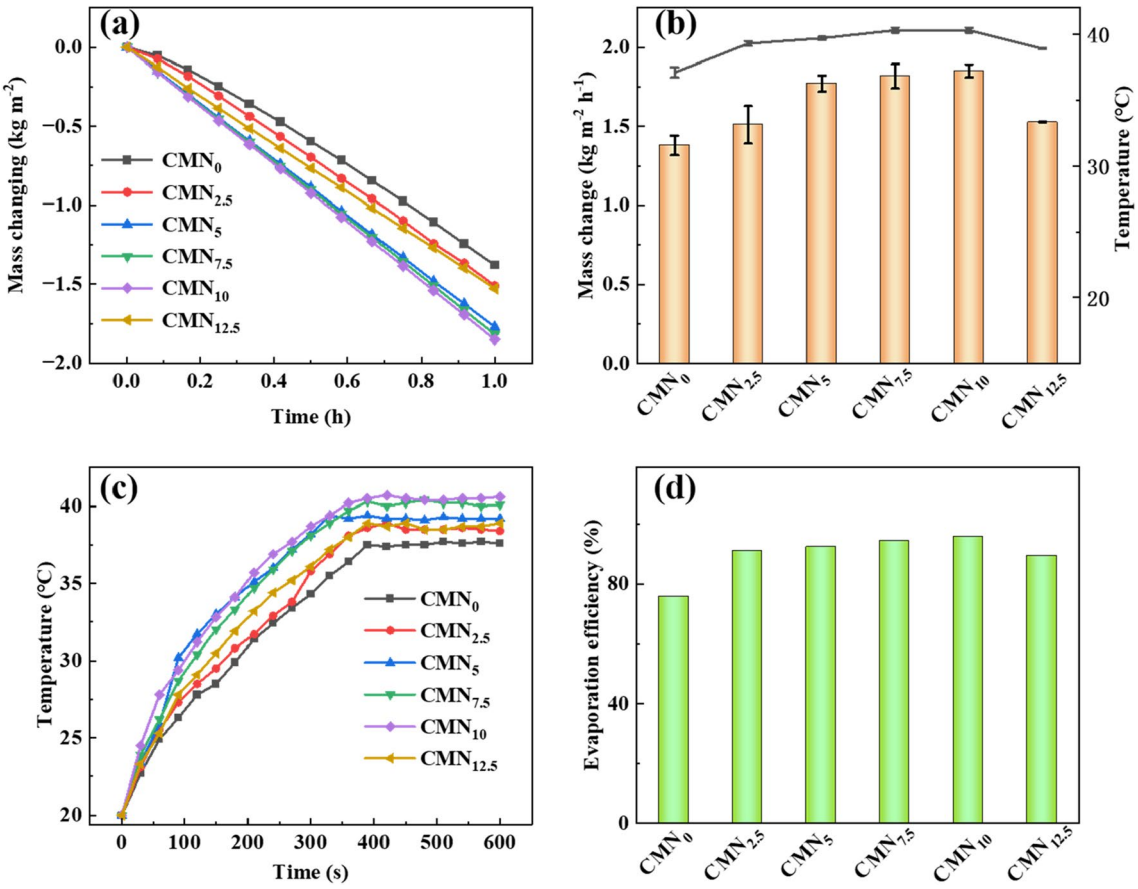

Fig. 5 **a** The mass changes of water over time; **b** evaporation rates and surface temperatures; **c** temperature rise curves; **d** solar evaporation efficiency of CMN_0, $CMN_{2.5}$, CMN_5, $CMN_{7.5}$, CMN_{10} and $CMN_{12.5}$

P-Ni chain. Good stability is significantly critical in practical application of the sample.

CMN_{10} was screened for the following seawater desalination experiment based on the above optimal water evaporation. Under one sun irradiation (1 kW m^{-2}), pure water, simulated seawater, 7 wt%, 10 wt%, and 20 wt% NaCl solution were, respectively, used for desalination performance test. As shown in Fig. 6a–b, salt concentration has little effect on its evaporation rate, even in solution with 20 wt% NaCl concentration, the evaporation rate of CMN_{10} can still reach 1.72 kg m^{-2} h^{-1}, which is only reduced by 7.03%. This also proved that CMN_{10} has a high salt tolerance. The cycle stability of CMN_{10} in seawater was measured with simulated seawater. As demonstrated in Fig. 6c, the water evaporation rate of CMN_{10} stabilized at 1.71 kg m^{-2} h^{-1} after 10 cycles. The above experiments showed that CMN aerogel has excellent cyclic stability and salt tolerance and CMN aerogel is a potential candidate for seawater evaporation in real environments.

The water vapor evaporation rate of CMN_{10} under different light intensities also performed (Figs. 6d, S9). As expected, the water evaporation rate of CMN_{10} aggrandized with light intensity increases, and it is 1.81, 3.41, and 4.95 kg m^{-2} h^{-1} under 1 sun, 2 sun and 3 sun irradiations, respectively. Obviously, there is no linear correlation between the evaporation rate and the light intensity. This could be ascribed to the increasing temperature difference between CMN_{10} surface and the environment with the increase in the light intensity; meanwhile, the thermal convection and radiation increase accordingly, resulting in energy loss.

Considering the complexity of real seawater, the evaporation rate of CMN_{10} in simulated seawater with different pH was further evaluated. As shown in Figs. 6e and S10, the actual water evaporation rate of CMN_{10} can still reach up to 1.74 and 1.73 kg m^{-2} h^{-1} in simulated seawater with pH 2 and 12, respectively. All the above evidence implied the stability and the practical application potential of CMN aerogel.

The rejection rate of metal ions is an important index of seawater desalination. Fig. S11 shows the experimental device for collecting the cooling water after the evaporation of simulated seawater. The ion concentration in cooling water was measured by inductively coupled plasma mass

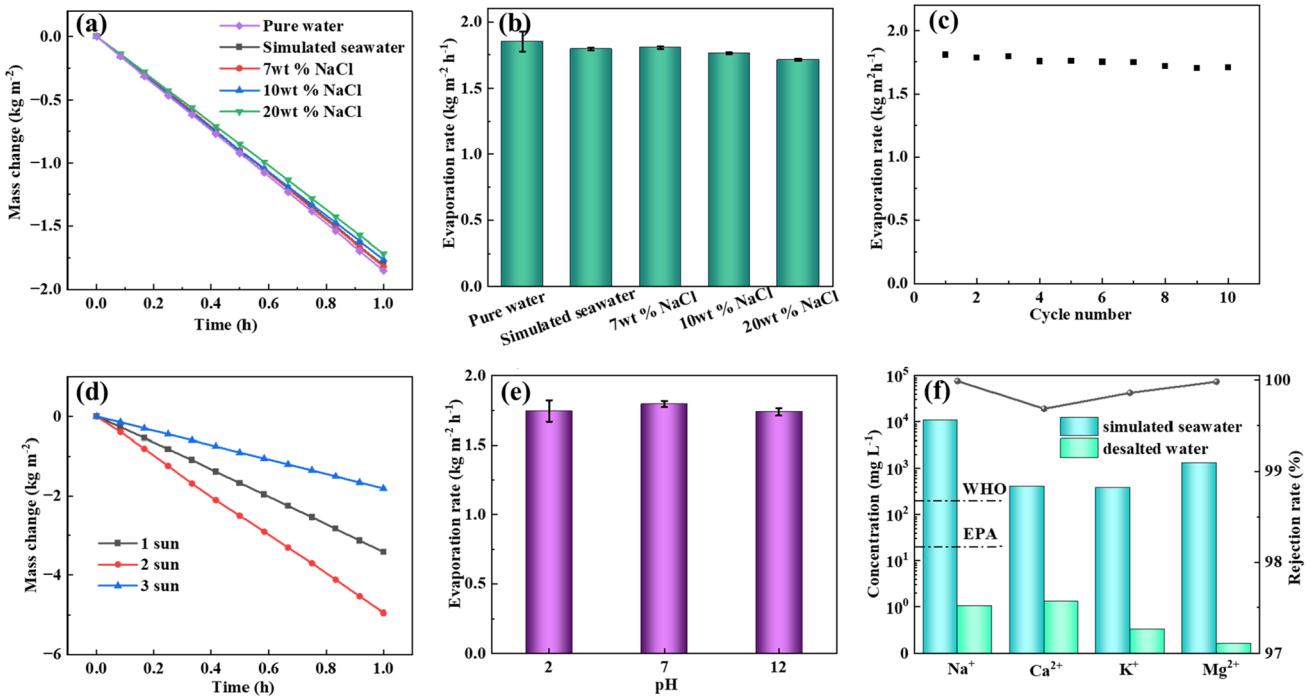

Fig. 6 CMN_{10} as an evaporator, **a** mass change curve and **b** evaporation rates of seawater from pure water, simulated seawater, 7 wt%, 10 wt%, 20 wt% NaCl solutions; **c** cycle stability of simulated seawater; **d** water mass change curves of simulated seawater at different light intensities; **e** water evaporation rates of simulated seawater at different pH values; **f** comparison of concentrations of major cations in simulated seawater before and after desalination

spectrometry (ICP-MS) to evaluate the seawater purification rate of CMN_{10}. As observed in Fig. 6f, Na^+ concentration decreased from 10,780 to 1.05 mg L^{-1}, which is far below the WHO standard of drinking water quality (200 mg L^{-1}) and the stricter requirements of the US Environmental Protection Agency (EPA) drinking water quality standards (20 mg L^{-1}). The rejection rate of Na^+ over CMN_{10} reached an astonishing 99.99%. As anticipated, the concentrations of Ca^{2+}, K^+, and Mg^{2+} in the collected cooling water were 1.29, 0.53, and 0.21 mg L^{-1}, respectively, also much lower than the WHO standard of drinking water quality, and the corresponding ions rejection rates reached 99.68%, 99.86% and 99.98%, respectively.

With the aggravation of environmental pollution, seawater desalination should pay more attention to the content of heavy metal ions and organic pollutants in cooling water. Therefore, the rejection ability of CMN_{10} was tested with Pd^{2+}, Cd^{2+}, and Cr^{2+} as model heavy metal ions. As displayed in Fig. 7a, the concentration of heavy metals in cooling water has significantly decreased, the concentration of Pd^{2+}, Cd^{2+}, and Cr^{2+} in cooling water is, respectively, 0.0007, 0.0013, 0.0005 mg L^{-1} and far below the drinking water requirements of WHO. The rejection rates of Pd^{2+}, Cd^{2+}, and Cr^{2+} by CMN_{10} are all above 99.98%. In addition, Rhodamine B, Congo red and Methylene blue were used as model organic pollution sources to test the rejection ability of CMN_{10} for organic pollutants in seawater. After CMN_{10} purification, the concentrations of Rhodamine B, Congo red and Methylene blue in cooling water were reduced to 0.0097, 0.0917 and 0.0098 mg L^{-1}, respectively, and the rejection rate reached more than 99.69% (Fig. 7b, c). The excellent rejection ability of dyes can be confirmed by the color differences in visual optical photographs (Fig. 7d–f). All these properties indicated that CMN materials have great potential in seawater desalination.

4 Conclusion

To sum up, CMN aerogel was successfully constructed by electrostatic self-assembly and hydrogen bond crosslinking. The rich pore structure provided by CNF not only facilitates the rapid escape of water vapor generated, but also produces multiple reflections of sunlight, thus enhancing the absorption of sunlight. Furthermore, the anchoring of P-Ni chain can effectively avoid the stacking of MXene layers and produce synergistic effect with MXene in the enhancement of the light absorption by CMN. CMN_{10} displayed high evaporation rates of 1.85 and 1.81 kg m^{-2} h^{-1} in pure water and simulated seawater, respectively. The rejection rate of metal ions (such as Na^+, Ca^{2+}, K^+, and Mg^{2+}; Pd^{2+}, Cd^{2+}, and Cr^{2+}) and organic pollutions

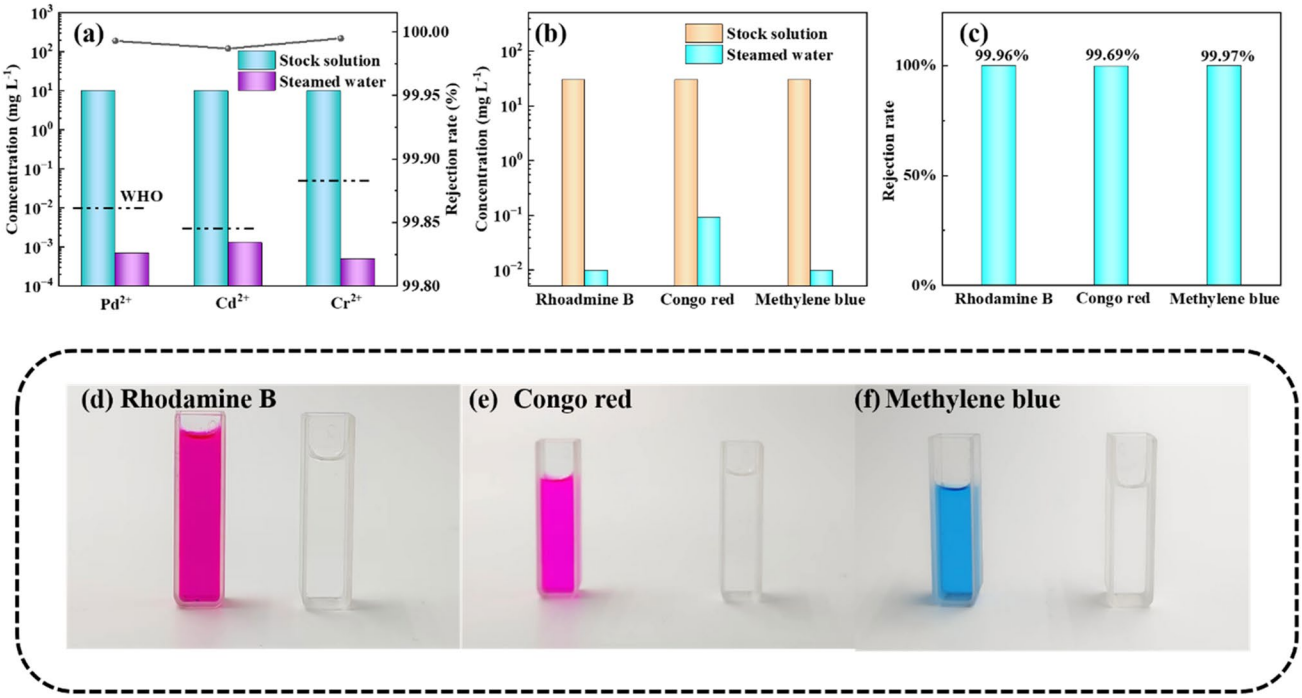

Fig. 7 CMN_{10} as evaporator, **a** concentration changes and rejection rates of heavy metal ions in simulated seawater; **b** concentration change before and after treatment, **c** rejection rate, and **d**–**f** digital photographs of organic pollutants

(Rhodamine B, Congo red and Methylene blue) in seawater was extremely satisfactory, and the obtained cooling water fully met the requirements of American drinking water quality standards. Most importantly, CMN_{10} is quite stable under complicated conditions, such as different salt concentrations, light intensity, and pH, which is of great significance for the actual desalination. This work is believed to shed new light on designing highly efficient seawater evaporation and purification materials for clean water production. Meanwhile, these functional nanocomposites can be used for other applications such as electromagnetic interference (EMI) shielding [54–58], energy usage [59–64], electronics [65–67], and coating for protecting metals [68].

Supplementary Information The online version contains supplementary material available at https://doi.org/10.1007/s42823-023-00540-0.

Funding This work was supported by the National Natural Science Foundation of China (no. 32071713), and the Outstanding Youth Foundation Project of Heilongjiang Province (JQ2019C001).

Declarations

Conflict of interest The authors declare that they have no conflict of interest.

References

1. Chiavazzo E (2022) Critical aspects to enable viable solar-driven evaporative technologies for water treatment. Nat Commun 13:5813. https://doi.org/10.1038/s41467-022-33533-0
2. Wu Q, Gao L, Huang M, Mersal G, Ibrahim M, El-Bahy Z, Shi X, Jiang Q (2022) Aminated lignin by ultrasonic method with enhanced arsenic (V) adsorption from polluted water. Adv Compos Hybrid Mater 5:1044–1053. https://doi.org/10.1007/s42114-022-00492-5
3. Li Z, Xie W, Yao F, Du A, Wang Q, Guo Z, Gu H (2022) Comprehensive electrocatalytic degradation of tetracycline in wastewater by electrospun perovskite manganite nanoparticles supported on carbon nanofibers. Adv Compos Hybrid Mater 5:2092–2105. https://doi.org/10.1007/s42114-022-00550-y
4. Sun Z, Zhang Y, Guo S, Shi J, Shi C, Qu K, Qi H, Huang Z, Murugadoss V, Huang M, Guo Z (2021) Confining FeNi nanoparticles in biomass-derived carbon for effectively photo-Fenton catalytic reaction for polluted water treatment. Adv Compos Hybrid Mater 5:1566–1581. https://doi.org/10.1007/s42114-022-00477-4
5. Xie K, Wei S, Alhadhrami A, Liu J, Zhang P, Elnaggar A, Zhang F, Mahmoud M, Murugadoss V, El-Bahy S, Wang F, Li C, Li G (2022) Synthesis of $CsPbBr_3$/CsP_b2B_r5@silica yolk-shell composite microspheres: precisely controllable structure and improved catalytic activity for dye degradation. Adv Compos Hybrid Mater 5:1423–1432. https://doi.org/10.1007/s42114-022-00520-4
6. Liu G, Yao G, Xu J, Yan X (2020) Spatial decoupling of light absorption and scattering centers in plasmon-assisted bubble

column evaporator for solar steam generation. ES Energy Environ 9:41–49. https://doi.org/10.30919/esee8c450
7. Wang Y, Peng G, Sharshir S, Kandeal A, Yang N (2021) The weighted vvalues of solar evaporation's environment factors obtained by machine learning. ES Mater Manuf 14:87–94. https://doi.org/10.30919/esmm5f436
8. Ahmed F, Umar A, Kumar S, Shaalan N, Arshi N, Alam M, Hasan P, Ramay S, Khan R, Aljaafari A, Alshoaibi A (2023) Manganese dioxide nanoparticles/reduced graphene oxide nanocomposites for hybrid capacitive desalination. Adv Compos Hybrid Mater 6:19. https://doi.org/10.1007/s42114-022-00601-4
9. Kaur R, Goyat R, Singh J, Umar A, Chaudhry V, Akbar S (2023) An overview of membrane distillation technology: one of the perfect fighters for desalination. Eng Sci 21:771. https://doi.org/10.30919/es8d771
10. Khawaji AD, Kutubkhanah IK, Wie J-M (2008) Advances in seawater desalination technologies. Desalination 221:47–69. https://doi.org/10.1016/j.desal.2007.01.067
11. Ghim D, Jiang Q, Cao S, Singamaneni S, Jun Y-S (2018) Mechanically interlocked 1T/2H phases of MoS_2 nanosheets for solar thermal water purification. Nano Energy 53:949–957. https://doi.org/10.1016/j.nanoen.2018.09.038
12. Xu R, Wei N, Li Z, Song X, Li Q, Sun K, Yang E, Gong L, Sui Y, Tian J, Wang X, Zhao M, Cui H (2021) Construction of hierarchical 2D/2D Ti_3C_2/MoS_2 nanocomposites for high-efficiency solar steam generation. J Colloid Interface Sci 584:125–133. https://doi.org/10.1016/j.jcis.2020.09.052
13. Hou Q, Xue C, Li N, Wang H, Chang Q, Liu H, Yang J, Hu S (2019) Self-assembly carbon dots for powerful solar water evaporation. Carbon 149:556–563. https://doi.org/10.1016/j.carbon.2019.04.083
14. Qin D-D, Zhu Y-J, Chen F-F, Yang R-L, Xiong Z-C (2019) Self-floating aerogel composed of carbon nanotubes and ultralong hydroxyapatite nanowires for highly efficient solar energy-assisted water purification. Carbon 150:233–243. https://doi.org/10.1016/j.carbon.2019.05.010
15. Zhao F, Zhou X, Shi Y, Qian X, Alexander M, Zhao X, Mendez S, Yang R, Qu L, Yu G (2018) Highly efficient solar vapour generation via hierarchically nanostructured gels. Nat Nanotechnol 13:489–495. https://doi.org/10.1038/s41565-018-0097-z
16. Meng S, Gong T, Zhao X, Tang C-Y, Yu P, Bao R-Y, Ke K, Liu Z-Y, Yang M-B, Yang W (2021) Boosting solar steam generation in dynamically tunable polymer porous architectures. Polymer 226:123811. https://doi.org/10.1016/j.polymer.2021.123811
17. Chen C, Liu H, Wang H, Zhao Y, Li M (2021) A scalable broadband plasmonic cuprous telluride nanowire-based hybrid photothermal membrane for efficient solar vapor generation. Nano Energy 84:105868. https://doi.org/10.1016/j.nanoen.2021.105868
18. Gao M, Peh CK, Phan HT, Zhu L, Ho GW (2018) Solar absorber gel: localized macro-nano heat channeling for efficient plasmonic Au nanoflowers photothermic vaporization and triboelectric generation. Adv Energy Mater 8:1800711. https://doi.org/10.1002/aenm.201800711
19. Wang J, Li P, Yu P, Leydecker T, Bayer I, Losic D, Neogi A, Wang Z (20212) Efficient photothermal deicing employing superhydrophobic plasmonic MXene composites. Av Compos Hybrid Mater 5:3035–3044. https://doi.org/10.1007/s42114-022-00549-5
20. Yuan M, Feng X, Yan T, Chen J, Ma X, Cunha P, Lan S, Li Y, Zhou H, Wang Y (2022) Superparamagnetic iron oxide-enclosed hollow gold nanostructure with tunable surface plasmon resonances to promote near-infrared photothermal conversion. Adv Compos Hybrid Mater 5:2387–2398. https://doi.org/10.1007/s42114-022-00444-z
21. Xu D, Li Z, Li L, Wang J (2020) Insights into the photothermal conversion of 2D MXene nanomaterials: synthesis, mechanism, and applications. Adv Funct Mater 30:2000712. https://doi.org/10.1002/adfm.202000712
22. Zhang D, Shah D, Boltasseva A, Gogotsi Y (2022) MXenes for photonics. ACS Photonics 9:1108–1116. https://doi.org/10.1021/acsphotonics.2c00040
23. Ihsanullah I (2020) Potential of MXenes in water desalination: current status and perspectives. Nano Micro Lett 12:72. https://doi.org/10.1007/s40820-020-0411-9
24. Li Z, Xu R, Wei N, Song X, Yang E, Liu Q, Sui Y, Cui H (2020) 3D network structure and hydrophobic Ni-G-WO_{3-x} solar-driven interfacial evaporator for highly efficient steam generation. Sol Energy Mater Sol Cells 217:110593. https://doi.org/10.1016/j.solmat.2020.110593
25. Tang R, Wang H, Dong X, Zhang S, Zhang L, Dong F (2023) A ball milling method for highly dispersed Ni atoms on g-C_3N_4 to boost CO_2 photoreduction. J Colloid Interface Sci 630:290–300. https://doi.org/10.1016/j.jcis.2022.10.110
26. Wei J, Zhao R, Luo D, Lu X, Dong W, Huang Y, Cheng X, Ni Y (2023) Atomically precise $Ni_6(SC_2H_4Ph)_{12}$ nanoclusters on graphitic carbon nitride nanosheets for boosting photocatalytic hydrogen evolution. J Colloid Interface Sci 631:212–221. https://doi.org/10.1016/j.jcis.2022.11.010
27. Zhu S, Lei Z, Dou Y, Lou C-W, Lin J-H, Li J (2023) Sputter-deposited nickel nanoparticles on Kevlar fabrics with laser-induced graphene for efficient solar evaporation. Chem Eng J 452:139403. https://doi.org/10.1016/j.cej.2022.139403
28. Yu X, Wang X, Zhang Q, Li J, Liu J (2014) Oxidation-resistant, solution-processed plasmonic Ni nanochain-SiO_x($x < 2$) selective solar thermal absorbers. J Appl Phys 116:073508. https://doi.org/10.1063/1.4893656
29. Yang B, Li C, Wang Z, Dai Q (2022) Thermoplasmonics in solar energy conversion: materials, nanostructured designs, and applications. Adv Mater 34:e2107351. https://doi.org/10.1002/adma.202107351
30. Cao S, Rathi P, Wu X, Ghim D, Jun YS, Singamaneni S (2021) Cellulose nanomaterials in interfacial evaporators for desalination: a "natural" choice. Adv Mater 33:e2000922. https://doi.org/10.1002/adma.202000922
31. Li J, Cui Y, Xiu H, Wang W, Du M, Yang X, Xu Q, Kozliak E, Ji Y (2022) An integrative cellulose-based composite material with controllable structure and properties for solar-driven water evaporation. Cellulose 29:2461–2477. https://doi.org/10.1007/s10570-022-04442-8
32. Han S, Yang J, Li X, Li W, Zhang X, Koratkar N, Yu ZZ (2020) Flame synthesis of superhydrophilic carbon nanotubes/Ni foam decorated with Fe_2O_3 nanoparticles for water purification via solar steam generation. ACS Appl Mater Interfaces 12:13229–13238. https://doi.org/10.1021/acsami.0c00606
33. Zhang C, Yuan B, Liang Y, Yang L, Bai L, Yang H, Wei D, Wang W, Chen H (2021) Solar vapor generator: a natural all-in-one 3D system derived from cattail. Sol Energy Mater Sol Cells 227:111127. https://doi.org/10.1016/j.solmat.2021.111127
34. Li W, Tian X, Li X, Liu J, Li C, Feng X, Shu C, Yu ZZ (2022) An environmental energy-enhanced solar steam evaporator derived from MXene-decorated cellulose acetate cigarette filter with ultrahigh solar steam generation efficiency. J Colloid Interface Sci 606:748–757. https://doi.org/10.1016/j.jcis.2021.08.043
35. Ghanbari R, Nazarzadeh Zare E, Paiva-Santos AC, Rabiee N (2022) $Ti_3C_2T_x$ MXene@MOF decorated polyvinylidene fluoride membrane for the remediation of heavy metals ions and desalination. Chemosphere 311:137191. https://doi.org/10.1016/j.chemosphere.2022.137191
36. Jia X, Liu X, Guan H, Fan T, Chen Y, Long Y-Z (2023) A loofah-based photothermal biomass material with high salt-resistance for efficient solar water evaporation. Compos Commun 37:101430. https://doi.org/10.1016/j.coco.2022.101430

37. Zhang Y, Guo X, Liao S, Wu D, Lv P, Wei Q (2022) Multi-scale structure synergistic strategy: a transpiration inspired hierarchical aerogel evaporator for highly efficient solar-driven clean water production. J Environ Chem Eng 10:107934. https://doi.org/10.1016/j.jece.2022.107934
38. Guo Y, Wang D, Bai T, Liu H, Zheng Y, Liu C, Shen C (2021) Electrostatic self-assembled $NiFe_2O_4/Ti_3C_2T_x$ MXene nanocomposites for efficient electromagnetic wave absorption at ultralow loading level. Adv Healthc Mater 4:602–613. https://doi.org/10.1007/s42114-021-00279-0
39. Xin W, Ma M-G, Chen F (2021) Silicone-coated MXene/cellulose nanofiber aerogel films with photothermal and joule heating performances for electromagnetic interference shielding. Adv Healthc Mater 4:7234–7243. https://doi.org/10.1021/acsanm.1c01185
40. Qin L, Yang D, Zhang M, Zhao T, Luo Z, Yu ZZ (2021) Superelastic and ultralight electrospun carbon nanofiber/MXene hybrid aerogels with anisotropic microchannels for pressure sensing and energy storage. J Colloid Interface Sci 589:264–274. https://doi.org/10.1016/j.jcis.2020.12.102
41. Tang L, Zhao X, Feng C, Bai L, Yang J, Bao R, Liu Z, Yang M, Yang W (2019) Bacterial cellulose/MXene hybrid aerogels for photodriven shape-stabilized composite phase change materials. Sol Energy Mater Sol Cells 203:110174. https://doi.org/10.1016/j.solmat.2019.110174
42. Li X, Wen C, Yang L, Zhang R, Li X, Li Y, Che R (2021) MXene/FeCo films with distinct and tunable electromagnetic wave absorption by morphology control and magnetic anisotropy. Carbon 175:509–518. https://doi.org/10.1016/j.carbon.2020.11.089
43. Wu X, Huang J, Gu H, Li N, Wang Y, Chen G, Dong C, Guan H (2022) Ternary MXene/MnO_2/Ni composites for excellent electromagnetic absorption with tunable effective absorption bandwidth. J Alloys Compd 911:165122. https://doi.org/10.1016/j.jallcom.2022.165122
44. Mao L, Hu S, Gao Y, Wang L, Zhao W, Fu L, Cheng H, Xia L, Xie S, Ye W, Shi Z, Yang G (2020) Biodegradable and electroactive regenerated bacterial cellulose/MXene ($Ti_3C_2T_x$) composite hydrogel as wound dressing for accelerating skin wound healing under electrical stimulation. Adv Healthc Mater 9:e2000872. https://doi.org/10.1002/adhm.202000872
45. Wang L, Song P, Lin CT, Kong J, Gu J (2020) 3D shapeable, superior electrically conductive cellulose nanofibers/$Ti_3C_2T_x$ MXene aerogels/epoxy nanocomposites for promising EMI shielding. Research 2020:4093732. https://doi.org/10.34133/2020/4093732
46. Zhai J, Cui C, Li A, Guo R, Cheng C, Ren E, Xiao H, Zhou M, Zhang J (2022) Waste cotton Fabric/MXene composite aerogel with heat generation and insulation for efficient electromagnetic interference shielding. Ceram Int 48:13464–13474. https://doi.org/10.1016/j.ceramint.2022.01.224
47. Ahmad Wani T, Garg P, Bera S, Bhattacharya S, Dutta S, Kumar H, Bera A (2022) Narrow-Bandgap $LaMO_3$ (M = Ni, Co) nanomaterials for efficient interfacial solar steam generation. J Colloid Interface Sci 612:203–212. https://doi.org/10.1016/j.jcis.2021.12.158
48. Zong Z, Ren P, Guo Z, Wang J, Chen Z, Jin Y, Ren F (2022) Three-dimensional macroporous hybrid carbon aerogel with heterogeneous structure derived from MXene/cellulose aerogel for absorption-dominant electromagnetic interference shielding and excellent thermal insulation performance. J Colloid Interface Sci 619:96–105. https://doi.org/10.1016/j.jcis.2022.03.136
49. Nguyen TKT, Dao QK, Tanaka D, Nghiem LHT, Nguyen MV, Nguyen ZH, Pham TT (2021) Flexible, affordable and environmentally sustainable solar vapor generation based on ferric tannate/bacterial cellulose composite for efficient desalination solutions. RSC Adv 11:31641–31649. https://doi.org/10.1039/d1ra05558e
50. Ni A, Fu D, Lin P, Xia Y, Pei D, Han X, Hua S, Li S, Zhang T (2022) Rapid fabrication of porous photothermal hydrogel coating for efficient solar-Driven water purification. ACS Appl Mater Interfaces 14:44809–44820. https://doi.org/10.1021/acsami.2c12073
51. Jiang Y, An N, Sun Q, Guo B, Wang Z, Zhou W, Gao B, Li Q (2022) Biomass hydrogels combined with carbon nanotubes for water purification via efficient and continuous solar-driven steam generation. Sci Total Environ 837:155757. https://doi.org/10.1016/j.scitotenv.2022.155757
52. Li Z, Wang C (2020) Novel advances in metal-based solar absorber for photothermal vapor generation. Chin Chem Lett 31:2159–2166. https://doi.org/10.1016/j.cclet.2019.09.030
53. Li D, Zhong H (2023) Facile engineering 3-D photothermal laser induced graphene for efficient steam generation. Sol Energy Mater Sol Cells 250:112104. https://doi.org/10.1016/j.solmat.2022.112104
54. Dai B, Ma Y, Dong F, Yu J, Ma M, Thabet H, El-Bahy S, Ibrahim M, Huang M, Seok I, Roymahapatra G, Naik N, Xu B, Ding J, Li T (2022) Overview of MXene and conducting polymer matrix composites for electromagnetic wave absorption. Adv Compos Hybrid Mater 5:704–754. https://doi.org/10.1007/s42114-022-00510-6
55. Wu N, Zhao B, Chen X, Hou C, Huang M, Alhadhrami A, Mersal G, Ibrahim M, Tian J (2022) Dielectric properties and electromagnetic simulation of molybdenum disulfide and ferric oxide-modified Ti3C2TX MXene hetero-structure for potential microwave absorption. Adv Compos Hybrid Mater 5:1548–1556. https://doi.org/10.1007/s42114-022-00490-7
56. Cheng H, Pan Y, Chen Q, Che R, Zheng G, Liu C, Shen C, Liu X (2021) Ultrathin flexible poly(vinylidene fluoride)/MXene/silver nanowire film with outstanding specific EMI shielding and high heat dissipation. Adv Compos Hybrid Mater 4:505–513. https://doi.org/10.1007/s42114-021-00224-1
57. Guo Y, Wang D, Bai T, Liu H, Zheng Y, Liu C, Shen C (2021) Electrostatic self-assembled $NiFe_2O_4/Ti_3C_2Tx$ MXene nanocomposites for efficient electromagnetic wave absorption at ultralow loading level. Adv Compos Hybrid Mater 4:602–613. https://doi.org/10.1007/s42114-021-00279-0
58. Gao Q, Pan Y, Zheng G, Liu C, Shen C, Liu X (2021) Flexible multilayered MXene/thermoplastic polyurethane films with excellent electromagnetic interference shielding, thermal conductivity, and management performances. Adv Compos Hybrid Mater 4:274–285. https://doi.org/10.1007/s42114-021-00221-4
59. Cao Y, Weng M, Mahmoud M, Elnaggar A, Zhang L, El Azab I, Chen Y, Huang M, Huang J, Sheng X (2022) Flame-retardant and leakage-proof phase change composites based on MXene/polyimide aerogels toward solar thermal energy harvesting. Adv Compos Hybrid Mater 5:1253–1267. https://doi.org/10.1007/s42114-022-00504-4
60. Bi X, Li M, Zhou G, Liu C, Huang R, Shi Y, Xu B, Guo Z, Fan W, Algadi H, Ge S (2023) High-performance flexible all-solid-state asymmetric supercapacitors based on binder-free MXene/cellulose nanofiber anode and carbon cloth/polyaniline cathode. Nano Res. https://doi.org/10.1007/s12274-023-5586-1
61. Yan Z, Li J, Chen Q, Chen S, Luo L, Chen Y (2022) Synthesis of $CoSe_2$/Mxene composites using as high-performance anode materials for lithium-ion batteries. Adv Compos Hybrid Mater 5:2977–2987. https://doi.org/10.1007/s42114-022-00524-0
62. Pathak M, Rout C (2022) Hierarchical $NiCo_2S_4$ nanostructures anchored on nanocarbons and $Ti_3C_2T_x$ MXene for high-performance flexible solid-state asymmetric supercapacitors. Adv Compos Hybrid Mater 5:1404–1422. https://doi.org/10.1007/s42114-022-00466-7
63. Pu L, Zhang J, Jiresse N, Gao Y, Zhou H, Naik N, Gao P, Guo Z (2022) N-doped MXene derived from chitosan for the highly effective electrochemical properties as supercapacitor. Adv

Compos Hybrid Mater 5:356–369. https://doi.org/10.1007/s42114-021-00371-5
64. Wei Y, Luo W, Zhuang Z, Dai B, Ding J, Li T, Ma M, Yin X, Ma Y (2021) Fabrication of ternary MXene/MnO_2/polyaniline nanostructure with good electrochemical performances. Adv Compos Hybrid Mater 4:1082–1091. https://doi.org/10.1007/s42114-021-00323-z
65. Kong D, El-Bahy Z, Algadi H, Li T, El-Bahy S, Nassan M, Li J, Faheim A, Li A, Xu C, Huang M, Cui D, Wei H (2022) Highly sensitive strain sensors with wide operation range from strong MXene-composited polyvinyl alcohol/sodium carboxymethyl-cellulose double network hydrogel. Adv Compos Hybrid Mater 5:1976–1987. https://doi.org/10.1007/s42114-022-00531-1
66. Wang J, Li P, Yu P, Leydecker T, Bayer I, Losic D, Neogi A (2022) Wang Z (2022) Efficient photothermal deicing employing superhydrophobic plasmonic MXene composites. Adv Compos Hybrid Mater 5:3035–3044. https://doi.org/10.1007/s42114-022-00549-5
67. Shao Y, Zhu Y, Zheng R, Wang P, Zhao Z, An J (2022) Highly sensitive and selective surface molecularly imprinted polymer electrochemical sensor prepared by Au and MXene modified glassy carbon electrode for efficient detection of tetrabromobisphenol A in water. Adv Compos Hybrid Mater 5:3104–3116. https://doi.org/10.1007/s42114-022-00562-8
68. He X, Li S, Shen R, Ma Y, Zhang L, Sheng X, Chen Y, Xie D, Huang J (2022) A high-performance waterborne polymeric composite coating with long-term anti-corrosive property based on phosphorylation of chitosan-functionalized $Ti_3C_2T_x$ MXene. Adv Compos Hybrid Mater 5:1699–1711. https://doi.org/10.1007/s42114-021-00392-0